Dynamics in Natural and Designed Elastins and Their Relation to Elastic Fiber Structure and Recoil

M. F. C. A. Carvajal,[‡] *J. M. Preston,*[†] *N. M. Jamhawi,*[‡] *T. M. Sabo,*

J. M. Aramini,[¶] *R. J. Wittebort,**[‡] *and R. L. Koder**[†,⊥]

ABSTRACT: Elastin fibers assemble in the extracellular matrix from the precursor protein tropoelastin and provide the flexibility and spontaneous recoil required for arterial function. Unlike many proteins, a structure-function mechanism for elastin has been elusive. We have performed detailed NMR relaxation studies of the dynamics of the minielastin **24x′** in solution and of purified bovine elastin fibers in the presence and absence of mechanical stress. The low sequence complexity of **24x′** enables us to determine dynamical timescales and degrees of local ordering with residue-specific resolution in the cross-link and hydrophobic modules using NMR relaxation. We find an extremely high degree of disorder, with order parameters for the entirety of the hydrophobic domains near zero, resembling that of simple chemical polymers and less than the order parameters that have been observed in other intrinsically disordered proteins. We find that backbone order parameters in natural, purified elastin fibers are comparable to those found in **24x′** in solution. The difference in dynamics, compared to **24x′**, is that backbone correlation times are significantly slowed in purified elastin. Moreover, when elastin is mechanically stretched, the high chain disorder in purified elastin is retained - showing that any change in local ordering is below that detectable in our experiment. Combined with our previous finding of a 10-fold increase in the ordering of water when fully hydrated elastin fibers are stretched by 50%, these results support the hypothesis that stretch induced solvent ordering, i.e. the hydrophobic effect, is a key player in the elastic recoil of elastin.

KEYWORDS: NMR, IDP, minielastin, elastin, relaxation

SIGNIFICANCE

Elastin is responsible for the spontaneous recoil of atrial walls that is necessary for cardiovascular function. Despite this critical role, the mechanism driving entropic recoil has remained unclear. Elastin is unusual in that it is intrinsically disordered in both soluble and fibrous forms. Using NMR, we have determined the timescales and amplitudes of dynamics in a soluble elastin mimetic and in cross-linked elastin in both relaxed and stretched states. Although dynamical timescales are different, both the soluble elastin mimetic and fibrillar elastin display an exceptionally high degree of disorder. No detectable increase in protein ordering was observed upon stretching, suggesting that entropic recoil is primarily driven by the hydrophobic effect and not configurational entropy loss.

INTRODUCTION

Elastin, an extracellular matrix protein that is the principal elastic protein in vertebrates, is abundantly expressed in blood vessels, lung tissue, ligaments, and skin (1). The mature elastic matrix is formed when tropoelastin, one of the most hydrophobic proteins found in nature, is exported to the extracellular matrix and consecutively undergoes an oligomerization transition known as coacervation, followed by cross-linking via the enzymatic oxidation of lysyl ε-amino groups (2). The reversible entropic elasticity of fully matured elastin fibers in blood vessel walls is responsible for elastic energy storage during the cardiac cycle and the dampening of pulsatile flow in distal arteries via the Windkessel effect (3). Elastogenesis terminates in adolescence, and in the course of a human lifetime, arterial elastin undergoes in excess of 10^7

stretching/contracting cycles. Oxidative damage accrued over human elastin's 70-year half-life reduces blood vessel compliance, resulting in hypertension, vascular calcification, ventricular hypertrophy, renal dysfunction and stroke (4). It is critical to understand the structural and dynamic origin of elastin's entropic elasticity in order to understand how this oxidative structural damage leads to the pathogenesis and progression of these diseases.

Elastin proteins are organized in alternating proline-rich hydrophobic domains and alanine-rich cross-linking domains (5). The hydrophobic domains are quasi-repeats of three to seven amino acids rich in hydrophobic residues including proline, whereas the alanine-rich cross-linking domains are weakly helical (6) and present the cross-linking lysine residues in close proximity at *i* and *i+3* or *i+4* positions (7). The elastic function of elastin proteins primarily arises from the hydrophobic domains. These were for some time thought to have a stable repeating type II β-turn secondary structure (8). However, we have shown using nuclear magnetic resonance (NMR) analyses of both natural elastin fibers (9) and simplified designed minielastin proteins (6) that these domains are intrinsically disordered in the unstressed relaxed state (9).

The entropically-driven recoil of a stretched disordered polymer can have two different origins: configurational entropy gain similar to that of vulcanized rubber (10), or the reduction of hydrophobic side chain exposure as the domain contracts and becomes more compact (11, 12). It is an important open question to what extent each of these mechanisms contribute to elastin function. In order to answer this question, we have performed detailed NMR studies of the dynamics of a minielastin, **24x′**, in solution and of purified bovine elastin in the presence and

absence of mechanical stress. Like natural elastin, **24x′** has an alternating structure of hydrophobic modules that flank cross-link modules and are at the termini.

Unlike natural elastin, **24x′** has identical repeats, which has allowed us to completely assign resonances in the protein (6). This has enabled us to determine the dynamical timescale(s) and the degree of local ordering with residue-specific resolution in the cross-link and hydrophobic modules of **24x′** from solution NMR relaxation studies (R_1, R_2 and NOE) at three field strengths. We find an extremely high degree of disorder resembling that of some simple chemical polymers and comparable to only the smallest order parameters observed in intrinsically disordered natural proteins (13-15).

We then examined the natural, purified elastomer using solid state ^{13}C NMR without magic angle spinning. Chain ordering was determined from the residual shielding anisotropy and dynamical timescales from R_1 and R_2 of the backbone carbonyl resonances. We find a similarly high degree of disorder in the natural protein and, importantly, mechanical stretching does not detectably decrease this disorder. As the polymer disorder we observe in both relaxed and stretched elastin is essentially identical, we infer that elastin's recoil does not arise from configurational entropy loss at the residue level.

THEORY

Dynamic analyses using R_1, R_2 and NOE data are less well developed for IDPs than for folded proteins. In both cases, the key function in the analysis is $J(\omega)$, the Fourier transform of the correlation function $c(t)$ for the dynamics that contribute to spin relaxation. $J(\omega)$ is related to R_1,

R_2 and NOE by three standard equations (SI eq's. 1a-c) (14, 16, 17). In the widely used Lipari-Szabo model-free approach (LS), c(t) is factored into independent dynamical modes, each of which is parameterized by an effective correlation time and a corresponding order parameter that are related to the timescale and amplitude of each dynamical mode, respectively (18, 19). LS has been used to analyze NMR relaxation in folded proteins and recently to analyze the 30 residue disordered terminus of an otherwise folded protein (14, 15). However, the general application of LS to IDPs has been questioned (20) and an alternative procedure, spectral density mapping (SDM), has also been used (21). In this method, the correlation function is not parameterized. Instead, the spectral density at five frequencies (0, ω_N, $\omega_H - \omega_N$, ω_H, and $\omega_H + \omega_N$) is determined from R_1, R_2 and NOE at two or more magnetic field strengths (20, 21). Insofar as SI eq.'s 1a-c are valid, SDM is rigorous. However, SDM does not directly relate to molecular properties such as the timescales and amplitudes of dynamical modes that are discussed next in the context of parameterized spectral densities. A useful test is to compare the parameterized spectral density with the spectral density map.

An adjunct to SDM that potentially provides greater physical insight is the general form of the correlation function, c(t), for a dynamical processes like diffusive or jump-like dynamics (22, 23):

$$c(t) = \frac{1}{5}\sum_{i=1}^{M} a_i\, e^{-t/\tau_i} \quad \text{and} \quad \sum_{i=1}^{M} a_i = 1 \qquad \text{eq. 1}$$

The spectral density is then

$$J(\omega) = 2\int_0^\infty c(t)cos\omega t dt = \frac{2}{5}\sum_{i=1}^{M} a_i L_i(\omega) \qquad \text{eq. 2}$$

and $L_i(\omega) = \tau_i / (1 + \omega^2\tau_i^2)$ is the usual Lorentzian function with correlation time τ_i. By constraining the correlation times to a range from 21 ps to 21 ns and separated by a factor of 4, Khan and co-workers have limited the general correlation function to 6 terms with 5 adjustable coefficients, a_i (24). A method for detecting the predominant correlation times in the spectral density has also been recently described (25). Here, we simply limit the number of terms in eq. 1 so that the minimum number of parameters required to fit the data within experimental errors is not exceeded. In this way, the timescales of the dynamical modes present in the system under study can be identified. Note that the coefficients specify the contribution of each dynamical mode to the total spectral density but not a physical property like the amplitude of a motion. To better understand the coefficients, a master equation for a specific dynamical model can be used (22). However, for even simple models, the number of terms in eq. 2 typically exceeds what is experimentally accessible. Ways to reduce this in the context of structured proteins have been discussed in detail(18, 19, 26) and those potentially relevant to IDPs are summarized next.

For IDPs in solution, the slowest motion is diffusional reorientation of the aggregate protein. Insofar as the correlation times for overall reorientation are greater by a factor of 10 or more than those for internal dynamics c(t) can be approximated as a product (19, 25, 27):

$$c(t) = c_0(t)c_I(t) \qquad \text{eq. 3}$$

where $c_o(t)$ and $c_I(t)$ are, respectively, the correlation function for overall and internal motions. For structured proteins that are not spherical, $c_o(t)$ is well approximated by a correlation function with two terms (19):

$$c_0(t) = \frac{1}{5}\left[Ae^{-t/\tau_{M1}} + (1-A)e^{-t/\tau_{M2}}\right] \qquad \text{eq. 4}$$

With A = 1, eq. 4 reduces to $c_o(t)$ for a spherical protein. Unlike structured proteins, IDPs have a flexible backbone and, in turn, a distribution of hydrodynamic radii. Consequently, there is a distribution of correlation times that is not easily obtained from NMR relaxation of backbone atoms which is dependent on both overall reorientation and large amplitude internal motions. Norton and coworkers circumvented this problem by assuming that the hydrodynamic radius, r_H, in the Stokes-Einstein equations for translational diffusion, $D_t = k_BT/6\pi\eta r_H$, and rotational diffusion, $D_r = k_BT/8\pi\eta r_H^3$, are the same (28). Importantly, D_t and thus the average hydrodynamic radius can be independently determined by PFG NMR or ultracentrifugation (6, 29). For IDPs with molecular weights comparable to **24x′**, the distribution of hydrodynamic radii is approximately gaussian with an average hydrodynamic radius, $\langle r_H \rangle$, that is found to be 4- to 7-fold greater than the gaussian width, σ, so that negative hydrodynamic radii are excluded (30, 31). With this distribution, $\langle r_H^n \rangle$ and $\langle r_H \rangle^n$ are equivalent within a few percent for n = -1, 1 and 3 and are used interchangeably herein. Thus, we calculate the average hydrodynamic radius from the translational diffusion constant:

$$\langle r_H \rangle = \frac{k_B T}{6\pi\eta D_t} \qquad \text{eq. 5a}$$

and, in turn, the average rotational correlation time is:

$$\langle\tau_M\rangle \equiv (6D_r)^{-1} = (\frac{4\pi\eta}{3k_BT})\langle r_H\rangle^3 \qquad \text{eq. 5b}$$

Averaging eq. 4 with a gaussian distribution and A = 1, we obtain:

$$c_0(t) = \frac{1}{5}\sum_{j=1}^{L} P_j^{eq} e^{-t/\tau_{M,j}}, \qquad \text{eq. 6a}$$

with:

$$P_j^{eq} = Ne^{-\left(\langle r_H\rangle - r_{H,j}\right)^2/2\sigma^2}\ ,\ N^{-1} = \sum_{j=1}^{L} e^{-\left(\langle r_H\rangle - r_{H,j}\right)^2/2\sigma^2}\ . \qquad \text{eq. 6b}$$

To account for internal dynamics with more than a single exponential correlation function, we use the 4-parameter $c_I(t)$ from the extended LS method (27):

$$c_I(t) = S^2 + (1 - S_F^2)e^{-t/\tau_F} + (S_F^2 - S^2)e^{-t/\tau_S}. \qquad \text{eq. 7}$$

S_i are the generalized order parameters and τ_i are effective correlation times for fast (F) and slow (S) internal motions, respectively. The three order parameters are constrained by the relation $S^2 = S_F^2 S_S^2$. In eq. 7, it is assumed that the fast and slow modes can be approximated as a single exponential correlation functions and that τ_F and τ_S differ by an order of magnitude or more (27). With these conditions, the order parameters (S_i^2), are equilibrium properties of the dynamics.

The total correlation function, eq. 3, is the product of eq.'s 6a and 7:

$$c(t) = \frac{1}{5}\sum_{j=1}^{L} P_j^{eq} e^{-t/\tau_{M,j}}\left[S^2 + (S_F^2 - S^2)e^{-t/\tau_S} + (1 - S_F^2)e^{-t/\tau_F}\right]. \qquad \text{eq. 8a}$$

Eq. 8a has 3L terms and is reduced to L+2 terms when overall reorientation is slow compared to internal dynamics, $\tau_{M,j} >> \tau_S$ and τ_F. After Fourier transformation, the result is:

$$J(\omega) = \frac{2}{5}\left[\left(S^2 \sum_{j=1}^{L} P_j^{eq} L_{M,j}\right) + (S_F^2 - S^2)L_S + (1 - S_F^2)L_F\right] \qquad \text{eq. 8b}$$

In the limit that $\tau_{M,j}$ are large compared to the reciprocal of the lowest NMR frequency (0.3 ns for the ^{15}N angular frequency at the lowest field in this study), eq. 8b reduces to three terms:

$$J(\omega) = \begin{cases} \frac{2}{5}\left[S^2\left(\frac{<\tau_M^{-1}>}{\omega^2}\right) + (S_F^2 - S^2)L_S + (1 - S_F^2)L_F\right], \ \omega \neq 0 \\ \frac{2}{5}[S^2 < \tau_M > + (S_F^2 - S^2)L_S + (1 - S_F^2)L_F], \ \omega = 0 \end{cases}, \qquad \text{eq. 8c}$$

with:

$$< \tau_M^{-1} >^{-1} \approx < \tau_M > = \sum_{j=1}^{L} P_j^{eq} \tau_{M,j} \qquad \text{eq. 8d}$$

In this limit, eq. 1 truncated to three terms and eq. 8c are formally equivalent with parameters related by,

$$\tau_1 = <\tau_M>,\ \tau_2 = \tau_S,\ \tau_3 = \tau_F,\ a_1 = S^2,\ a_2 = S_F^2 - S^2, \text{ and } a_3 = 1 - S_F^2 \qquad \text{eq's 9}$$

RESULTS

Backbone amide solvent exchange. To focus on motional dynamics, we first show that proton exchange at solvent exposed amides, known to affect NMR relaxation (32) is negligible in these experiments. Proton exchange rates were obtained using the CLEANEX-PM method (33) (Figure 1). While exchange rates of 10 s^{-1} to 30 s^{-1} increase R_2 by 20–30%, exchange rates at pH 6, Figure 1, are less than 2 s^{-1} and thus make negligible contributions to R_2 (32).

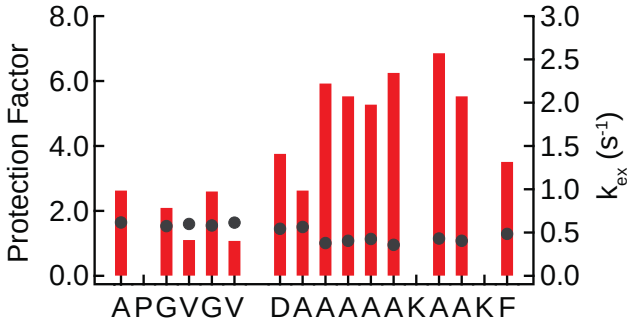

Figure 1. Amide proton exchange rates (filled circles) in the hydrophobic $(APGVGV)_7$, and cross-link, (DA_5KA_2KF), modules at pH 6 in **24x′**. The protection factors (bars) are calculated from the exchange rates as described by Englander and co-workers.[34]

Protection factors (red bars) calculated from the exchange rates (34, 35) are less than two for residues in hydrophobic modules and, systematically, somewhat higher than five for residues in the central portion of the cross-link module. Protection factors less than five indicate an absence of secondary structure (36). Thus, the absence of secondary structure in the hydrophobic

modules and weak ordering in the central residues of the cross-link modules that was previously concluded on the basis of chemical shifts and NOEs is in complete agreement with amide proton exchange rates.(6)

Backbone ^{15}N *relaxation parameters* measured at three NMR frequencies (500, 600 and 800 MHz) are shown graphically in Figure 2 with the complete data set listed in SI Table 1. Within experimental error, R_1, R_2 and NOE values are nearly independent of residue in the hydrophobic repeat and in residues 2–10 of the cross-link module with a difference between residues in the hydrophobic repeat and those in the cross-link module. Faster R_1 and R_2 relaxation rates and larger NOEs in the cross-link module indicate slower and/or more restricted motion than in the hydrophobic repeat consistent with our earlier chemical shift-based prediction of partial helical conformation in this region.(37) The small R_2 / R_1 ratios (~2 to ~3) in both hydrophobic repeat and cross-link residues indicate that fast motions (τ < 100 ps) affect spin relaxation more than much slower motions which include overall reorientation of the protein (τ > 10 ns). NOEs are frequency dependent and approach the slow-motion limit (NOE ~ 0.85) at 800 MHz. This indicates that dynamics with correlation time(s) shorter than that for overall reorientation and longer than that for fast backbone motions are also present.

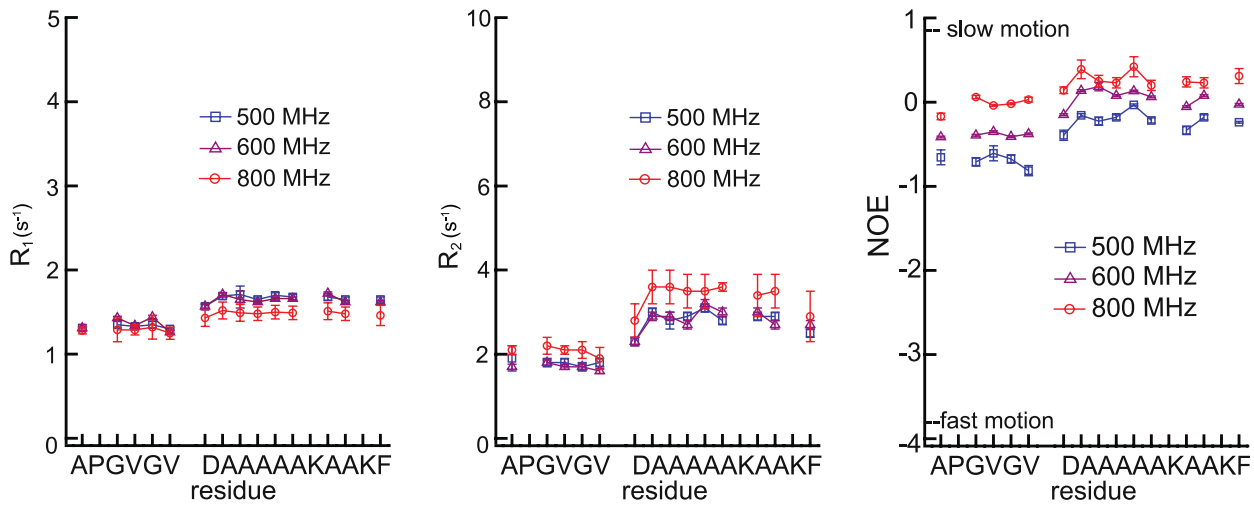

Figure 2. R_1, R_2 and NOE relaxation data at 500 MHz (blue), 600 (magenta) and 800 MHz (red). Cross-linker termini, residues 1 (D) and 11 (F), have intermediate relaxation parameters between those in the hydrophobic repeat and the cross-link module.

Fits of the relaxation data with eq. 1 with 3 terms and equation 8a are summarized in Figure 3. While R_1 and R_2 values could be fit with two-terms in eq. 1, the 3-parameter correlation function predicted NOEs that were less than the experimental values. This was resolved by adding a third term with an intermediate correlation time and an additional coefficient.(27) χ^2 surfaces for this 5-parameter fit with eq. 1 are shown for a representative residue, A1, in the hydrophobic repeat, Figure 3a-c. Residue specific parameters from this fit are shown in Figures 3d-g (red marks). Standard errors are typically ± 15% except for the slowest motion that is fit with τ_1 from 4 ns to more than 50 ns and a_1 from 0 to 0.15. However, within these ranges, the best fit values of τ_2, τ_3, a_2 and a_3 are essentially unchanged.

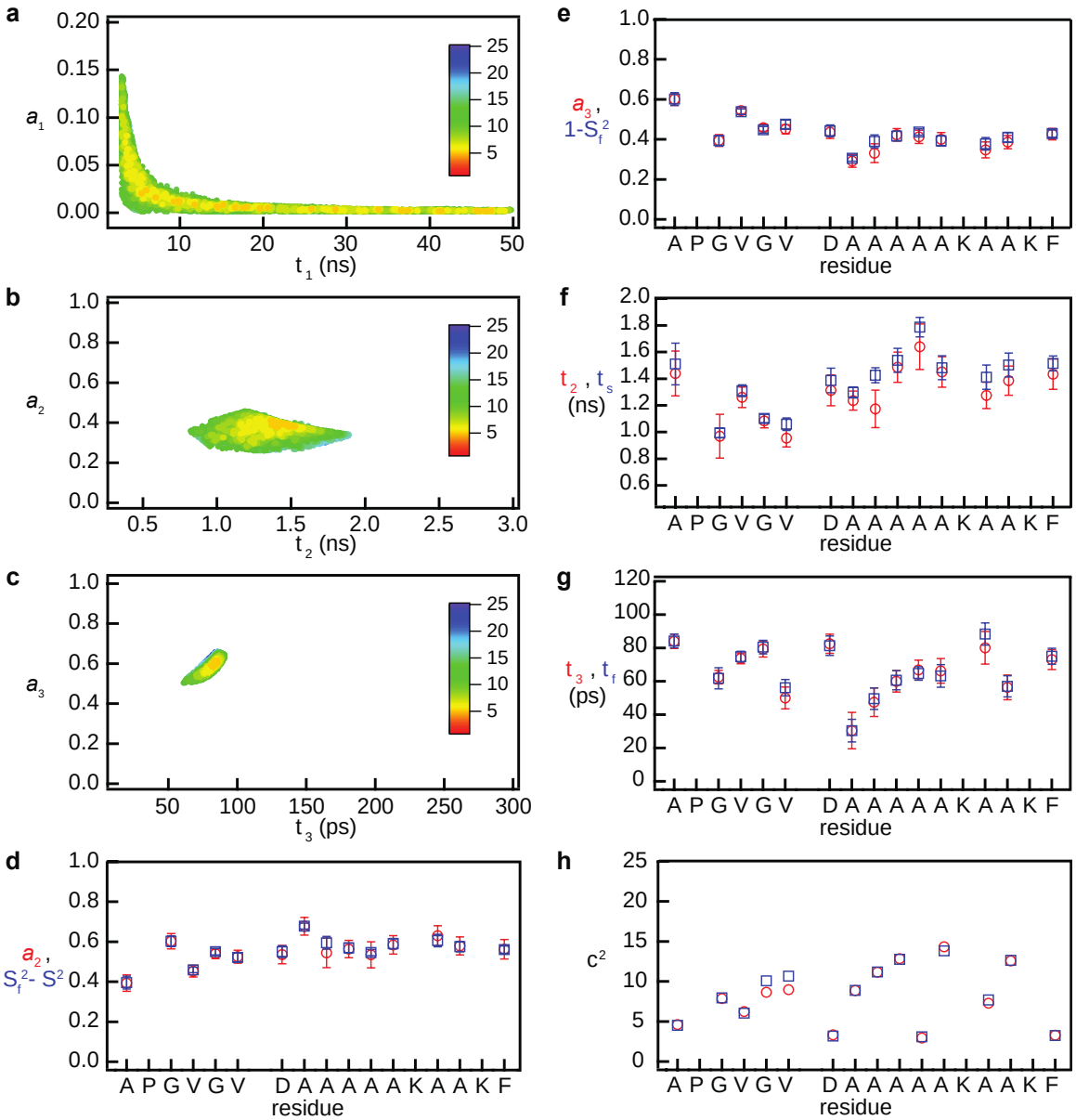

Figure 3. (**a-c**) χ^2 surfaces for the fit of the eq. 1 spectral density to the relaxation data from the first residue of the hydrophobic repeat (A1). **(d-g, red)** Fit parameters obtained using the three term Lorentzian (5 parameters), eq. 1. **(d-g, blue)** Fit obtained using eq. 8 (4 parameters). (**h)** Per residue χ^2 of the fits using eq. 1 (red) and eq. 8 (blue).

The protein studied here is an IDP and, compared to folded proteins of the same molecular weight, **24x′** has a distribution of expanded hydrodynamic radii. To account for this, we constrain the slowest correlation function to a gaussian distribution, eq. 8a, with the average hydrodynamic radius obtained from PFG NMR, 34 ± 2 Å,(6) and the gaussian width parameter, σ = 4.3 Å, that is estimated from other IDPs.(30, 31) Then, the average correlation time for overall reorientation is 36 ± 6 ns with values that range from ~20 ns to ~60 ns (gaussian probabilities greater than 0.05). With this constraint, the 4-parameter fit of eq. 8a to the relaxation data are shown graphically in Figures 3d-g (blue marks) and compiled in Table 3 of the supplemental data. We see that eq. 8 correlation times τ_S and τ_F are essentially equivalent to τ_2 and τ_3 obtained using eq. 1 truncated to three terms. Averaged over residues in the hydrophobic domain or residues in the cross-link domain, the correlation times are 1.2 ± 0.1 ns and 1.5 ± 0.1 ns for the slow internal motion or 73 ± 6 ps and 65 ± 7 ps for the fast internal motion, respectively. Standard errors in the residue specific parameters (Supplemental data, Table 3) are comparable to the standard deviations of the averages over parameters within each domain. Since $<\tau_M>$ is greater than 0.3 ns and the correlation times $<\tau_M>$, τ_S and τ_F differ by one or more orders of magnitude, the coefficients, a_i (eq. 1), are related to order parameters, S_i^2 (eq.'s 8), by eq.'s 9. A striking feature of our analysis is the nearly complete overall dynamic disorder, $S^2 = S_S^2 S_F^2 \sim 0$, of the backbone. This arises from the chain dynamic on two time scales with S_F^2= 0.51 ± 0.04 and S_F^2 = 0.60 ± 0.1 for residues in hydrophobic and cross-link domains, respectively. Because $S_S^2 = S^2 / S_F^2$, amplitudes of the slow internal motions are greater than the amplitude of the fast, internal motion.

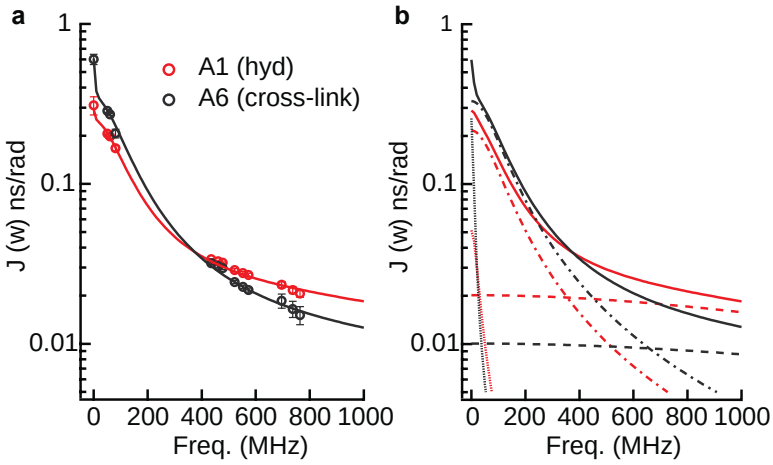

Figure 4. Logarithmic graphs of the spectral density versus NMR frequency. Red and black indicate A1 in the hydrophobic repeat and A6 in the center of the cross-link module, respectively. **(a)** The total spectral density obtained from eq. 8 with Figure 3 parameters (continuous curve) and SDM (circles). **(b)** Contributions to the total spectral density (continuous curves) from the terms with slow (···), intermediate (-·-) and fast (- -) correlation times.

Comparison of parameterized spectral densities with the Spectral density map. In Figure 4, the eq. 8 spectral density is compared with the spectral density map. Agreement is excellent in the frequency ranges where the two methods overlap, 0 to 200 MHz and 400 to 800 MHz. Both analyses show that the dynamics of residues in the hydrophobic modules are different from residues in the cross-link modules. Contributions to the eq. 8 spectral density from slow overall, slow internal and fast internal dynamics are shown in Figure 4b. At frequencies below 10 MHz, only dynamics with the slow and intermediate correlation times contribute to the total spectral density while the fast dynamics are dominant above 600 MHz. From 125 MHz to 200 MHz, dynamics with the intermediate correlation times are dominant.

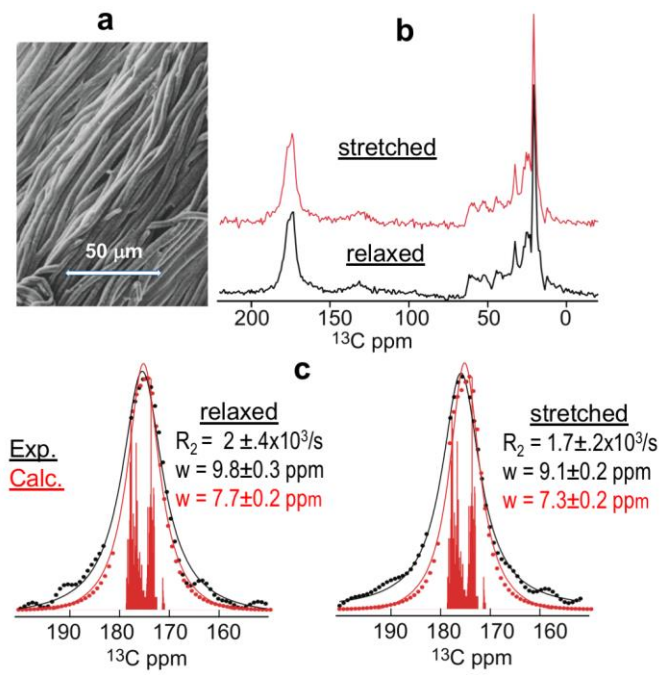

Figure 5. (a) Scanning electron micrograph of purified bovine elastin fibers. (b) Natural abundance ^{13}C NMR spectra of purified fibers, stretched (122%) and relaxed, obtained at 700 MHz using a solution NMR probe. (c) (•) ^{13}C carbonyl spectra of stretched (132%) and relaxed bovine elastin fibers obtained on a 500 MHz instrument. (•) Calculated stick spectra (red) convoluted with the indicated experimental R_2 values. Continuous curves (— , —) and w's are, respectively, Lorentzian fits and linewidths in ppm.

Dynamic analysis of purified bovine elastin. To compare the high degree of disorder in the minielastin in solution with that in purified bovine elastin (Figure 5a), relaxed and stretched (Figure 5b, c), we have used ^{13}C NMR without magic angle spinning (MAS). Without MAS, order parameters are measured directly from the contribution of residual shielding anisotropy to the observed linewidth, $\Delta\sigma_{res}$, with the relation $S = \Delta\sigma_{res}/\Delta\sigma_{stat}$(9) where $\Delta\sigma_{stat}$ is the static shielding anisotropy. We focus on ^{13}C backbone carbonyls (Figure 5c) because $\Delta\sigma_{stat}$ is large, ~ 128 ppm, and ~98% of the carbonyl groups are from the protein backbone. Spectra of stretched

and relaxed elastin, Figure 5b, are essentially superimposable with carbonyl linewidths, 9-10 ppm, that are small compared to the static pattern breadth, ~128 ppm. This indicates a high degree of dynamic disorder, in which case the contributions to the observed linewidth from R_2 broadening and the dispersion of isotropic shifts cannot be neglected. To account for the dispersion of isotropic shifts and R_2 relaxation, a ^{13}C spectrum of tropolastin carbonyl shifts was convoluted with the experimentally determined R_2 values and then fit to a Lorentzian, Figure 5c. Isotropic shifts were estimated for the bovine tropoelastin sequence (38) using the chemical shift protocol that predicted observed $^{13}C'$ shifts in **24x′** (6, 39). Then, $\Delta\sigma_{res}$ is the difference between the observed and calculated line-widths. We find that $\Delta\sigma_{res}$ is ~2 ppm in both stretched and relaxed states indicating that S for chain dynamics in the purified elastin is close to zero, i.e., not different than the small values of S^2 determined for **24x′** in our analysis of solution NMR relaxation data. Importantly, no change in the degree of the dynamic disorder was detected when the fiber is stretched.

Although protein backbones of **24x′** in solution and in the purified elastin are similarly disordered, their R_1 and R_2 values are quite different. Backbone carbonyl ^{13}C R_1 and R_2 values in elastin are 4-fold slower and three orders of magnitude faster, respectively. This cannot be explained by the difference in the nucleus probed and indicates significantly slower motions in the elastic matrix. To analyze the relaxation data, we apply eq. 8 in the limits of negligible chain ordering ($S^2 = 0$) and, due to cross-linking, quenched overall reorientation ($\tau_M \rightarrow$ infinity). The resulting expression has 3 parameters and was fit to R_1 and R_2 data obtained on 500 and 700 MHz instruments. Since R_1 and R_2 for stretched and relaxed elastin are equivalent within experimental error, their average was fit and S_F^2 was constrained to the range in **24x′,** $0.4 < S_F^2 <$

1. We find correlation times of τ_F = 380 ± 140 ps and τ_S = 1.7 ± 0.5 μs, i.e., slowing of the dynamics by at least factors of 4 and 10^3 compared to the soluble minielastin. While there is no significant change in ordering of the chains as a result of coacervation and cross-linking, dynamics are dramatically slowed.

DISCUSSION

We have used NMR methods to determine the timescales and amplitudes of dynamics in a soluble minielastin, **24x′**, and in purified elastin fibers. These results were obtained by analysis of combined NMR relaxation and PFG data using spectral density mapping, a general spectral density truncated to three Lorentzian functions and a modified Lipari-Szabo spectral density. We note that the relaxation data alone could not be fit to a spectral density with two Lorentzian functions. As has been seen before, the R_1 and R_2 data alone could be fit, but the predicted NOE's were more negative than the experimental values indicating the presence of dynamics with an intermediate correlation time.(27) With three Lorentzian terms, the correlation time for the slowest motion, τ_1, was poorly constrained by the relaxation data alone (4 ns < τ_1 < 60 ns). However, the correlation times τ_2, 1.2 ± 0.1 ns or 1.5 ± 0.1 ns, and τ_3, 73 ± 6 ps or 65 ± 7 ps, for residues in the hydrophobic or cross-link modules, respectively, were well constrained. Absent slow conformational exchange, the slowest correlation time is for overall reorientation of the protein. Using the hydrodynamic radius, 34 ± 2 Å, that we previously determined for **24x′** by PFG NMR and analytical ultracentrifugation (37), the average overall rotational correlation was constrained to 36 ns and a modified Lipari Szabo spectral density was fit to the relaxation data. Since overall motion is slow compared to the reciprocal of the lowest NMR frequency, the contribution to the spectral density from overall reorientation depends only on the average

correlation time, $<\tau_M>$. The spectral density obtained in this way is in excellent agreement with the spectral density map over wide frequency ranges indicating that it accounts for the available data and relating the amplitude factors for each of the dynamical modes to order parameters using using eq.'s 9 is appropriate because of the time-scale separations, τ_1, τ_2, and $<\tau_M>$ are separated by factors of ~20. The striking conclusion is that the overall amplitudes of the protein's backbone chain dynamics are large, $S^2 \sim 0$.

We find that backbone dynamics in **24x′** at individual residues occur on two times scales, τ_S = 1.0 to 1.8 ns and $\tau_F \sim$ 30 to 88 ps. Similar correlation times have been reported for backbone dynamics in well-structured proteins (40) and in IDP's including the disordered region of GCN4 (14), residues 146-199 of Engrailed 2 (24) and the disordered c-terminus of a Sendai virus protein (41). However, the range of S^2 values in **24x′**, 0.002 – 0.018, are significantly smaller than found in well-structured proteins ($S^2 \sim 0.85$ (17)) and comparable only to the most disordered residues at the N-terminus of the disordered region of the transcription factorGCN4 (14). We note that the disordered region of GCN4 folds upon DNA binding (42), whereas elastin retains complete disorder in the mature elastic matrix. Using eqns 9 from above to interpret the coefficients of the three-term correlation function used in the analysis of the viral protein (41), we find larger values of S^2 and S_f^2 indicating that this IDP is also more ordered than **24x'**. Another IDP analyzed in detail by NMR, Pdx1-C(43), has a high proline content: 22% compared to 14% in **24x'**. In Pdx1-C(43) the presence of negative C^α secondary shifts (43) indicates a propensity for forming extended 2° structures such as sheet and PPII. The high level of disorder in minielastin **24x'** observed using NMR relaxation is completely consistent with amide

hydrogen exchange rates (Figure 1) and our previous analysis of chemical shifts and ^{1}H NOEs (37).

We have also studied purified elastin using natural abundance ^{13}C NMR without magic angle spinning (MAS). While this experiment does not have residue specific resolution, the experiment provides an overall picture of the timescale and amplitude of carbonyl group dynamics and refines an earlier estimate obtained from ^{13}C NMR with MAS (9). Importantly, due to extensive cross-linking in natural elastin only chain dynamics are accessible. The order parameter for chain dynamics was directly estimated from the contribution of residual ^{13}C shielding anisotropy to the observed linewidths, 9.8 ± 0.3 ppm (relaxed) and 9.1 ± 0.2 ppm (stretched). However, the dominant contributions are from the observed R_2 relaxation rate and the estimated dispersion of isotropic shifts. Thus, residual shielding in both stretched and relaxed elastin is ~ 2 ppm and small compared to the static shielding of a polypeptide amide, 135 ppm, indicating an average backbone order parameter of S ~ 0.02 or S^2 ~ .004. Thus, S^2 for the protein backbone in purified elastin is essentially the same as for **24x′** in solution. This highly disordered structure of proteins with elastin-like sequences is found in solution, the coacervate and in the natural, cross-linked material (6, 9, 44). Compared to the minielastin in solution, dynamics are, however, significantly slowed in the cross-linked material. The long correlation time, τ_S, increases by a factor of 10^3 while τ_F is much less affected and increases by a factor of 4 suggesting that the slow motion corresponds to chain dynamics on the length scale of the spacing between cross-links and the fast motion on a shorter and more local length scale that would be less affected by crosslinks. The spacing between cross-links in elastin is the length of the

hydrophobic domains which varies from 11 to 55 residues. We conclude that structured regions in the elastin are either absent or constitute a small part of the protein.

A model of the elastin fibril has been previously described (45). It is based on a solution structure of tropoelastin deduced from small angle X-ray scattering and native cross-links found in an early study of elastin indicating that the domains coded by exons 10, 19 and 25 are cross-linked (46). A more recent and exhaustive study shows that the cross-links in bovine elastin are heterogeneous, i.e., all cross-link domains are linked in multiple ways (47). Here, we have directly observed the high degree of dynamic disorder that is required for random cross-linking. Elastin-like sequences are highly disordered in monomeric and fibrous forms on the ns and μs timescales, respectively, and this is different from other fibers. Collagen, for example, is folded (triple-helix) in both monomeric and fibrous forms while amyloid, like elastin, is an IDP when monomeric (48) but is folded in fibers (cross-β structure) (49, 50). The high disorder in elastin is a consequence of high proline content and low sequence complexity. The latter inhibits the efficient packing found in folded proteins and removal of proline leads to formation of β-sheets and amyloid (51).

In conclusion, we find that the very high chain disorder observed in solution is retained in mature, cross-linked elastin. Moreover, no evidence for increased local ordering of the protein backbone induced by mechanical stretch is observed. Previously, we reported a 10-fold increase of the ordering of water when fully hydrated elastin fibers are stretched by 50% (52). Together, these results support the hypothesis that stretch induced solvent ordering, i.e. the hydrophobic effect, is a key player in the elastic recoil of elastin (11, 12).

MATERIALS AND METHODS

Protein expression. ^{15}N-labelled samples of minielastin constructs with sequence 24′-x′-24′-x′-24′-x′-24′, where **24′** = $(APGVGV)_7$, and **x′** = DA_5KA_2KF, were expressed and prepared as described previously.(6) NMR samples were ~300 μM protein in pH 6, 50 mM phosphate buffer (90% H_2O / 10% D_2O).

Purification of elastin fibers from fresh bovine neck ligaments with a protocol(53) that yields pure elastin fibers with smooth surface and uniform diameter, Figure 5a. Briefly, samples of appropriate size for NMR were initially cut from the large ligament, washed with aqueous sodium chloride to remove water-soluble proteins and then with organic solvents to remove lipids. Other proteins were removed by treatment with cyanogen bromide (elastin has no methionine) followed by a wash with aqueous urea containing β-mercaptoethanol and final purification by limited trypsin digestion for 4 hours at 37 °C to remove micro-fibrillar components. Purified samples were stored at – 80 °C.

NMR data of 24x′ was collected on Bruker Avance 500, 600 and 800 MHz instruments equipped with cryoprobes. ^{15}N R_1 and R_2 relaxation rates and amide exchange rates (700 MHz) were measured at 25°C using pulse sequences in the manufacturer's pulse sequence libraries with the exception of R_2 at 600 MHz which was measured by Chemical exchange saturation transfer (CEST). R_1 spectra were recorded with ten delay times (10 to 1200 ms) and 2 s recycle delay and R_2 spectra with eight delays (10 to 350 ms) and 1 s recycle delay. NOE spectra were recorded with a 10 s saturation period and 4 s recycle delay. Acquisition parameters were 1024 and 200

complex points in direct and indirect dimensions, respectively, and 20 scans per t_1 increment. Data were processed using NMRPipe and TopSpin 3.5pI7 software. Relaxation rates were calculated using peak heights and steady-state [^{1}H]-^{15}N NOE values were calculated from the ratio of peak heights in NMR spectra acquired with and without proton saturation. The signal-to-noise ratio in each spectrum was used to estimate the experimental uncertainty. ^{15}N CEST spectra were recorded with a B_1 field of 87.5 +/- 4 Hz calibrated as previously described(54, 55), with an ^{1}H decoupling field strength of 3.5 kHz centered at 8.5 ppm during the mixing time (500 ms) and 70 B_1 offsets from 102 to 136.5 ppm. A reference experiment with a null mixing time was also acquired. The spectral parameters were 512 and 64 complex points in the direct and indirect dimensions, respectively, 4 scans per t_1 increment and a recycle delay of 1.5 sec. Data were plotted as normalized peak intensity (to the reference intensity) vs. offset and errors in the data points were estimated from the deviation of peak intensities where peak attenuation was not occurring. Calculation of R_1 and R_2 utilized an in-house python script (56-58).

Fit parameters of eq. 1 and 8 (Figure 3) were obtained via Monte Carlo simulation where calculated values greater than two standard deviations of the experimental values were excluded. Values of χ^2 for data fits were calculated using the following relation (59, 60):

$$\chi^2 = \sum\left[\left(\frac{R_{1,c}-R_{1,e}}{\sigma_{R_{1,c}}}\right)^2 + \left(\frac{R_{2,c}-R_{2,e}}{\sigma_{R_{2,c}}}\right)^2 - \left(\frac{NOE_c-NOE_e}{\sigma_{NOE_c}}\right)^2\right] \quad \text{eq. 10}$$

Subscripts “e” and “c” indicate experimental and calculated values respectively and the sum is over NMR frequencies.

Static ^{13}C NMR spectra of stretched and relaxed Elastin were obtained on a homebuilt 500 MHz spectrometer and a 700 MHz Varian Inova spectrometer. For the 500 MHz instrument, the ends of a dry elastin sample (~ 2 mm × 25 mm) were super-glued to ~2 cm lengths of 3.2 mm G10 rod. Following overnight equilibration in $^{2}H_2O$, the fiber assembly was inserted into a 5 cm length of a 5 mm NMR tube open at both ends. At one end, the rod was sealed to the glass tube with glue. So that the sample could be stretched, the rod protruding at the other end was held in place and sealed with parafilm. This assembly was inserted into the horizontal coil of the homebuilt probe.(61) R_1 and R_2 relaxation times were measured using inversion recovery and Hahn echo pulse sequences with relaxation delays of 4 s. An arrangement similar to the above was adapted for the unmodified cryoprobe of the 700 MHz instrument and a 5 mm sample tube with the closed end removed. G10 rods were cut to protrude from the ends of the NMR tube so that the elastin sample (2 mm × 29 mm) was centered in the sample coil. The lower rod was glued to the NMR tube and the upper rod was held in place with parafilm. R_1 spectra were recorded at nine delays (0.25 to 12 s) and R_2 spectra were recorded at ten delays (0.2 to 1.2 ms) with 4 s recycle delays.

ASSOCIATED CONTENT

Supporting Information

All reference to the supporting information is included in the main text. The following files are available free of charge. R_1, R_2 and NOE equations, relaxation data and fit parameters for **24x′,** CLEANEX data and relaxation data of purified elastin relaxed and stretched (PDF)

AUTHOR INFORMATION

Corresponding Authors

* dick.wittebort@louisville.edu

* rkoder@ccny.cuny.edu

Author Contributions

F.C.A.C., J.M.P., R.J.W., and R.L.K designed research; F.C.A.C., J.M.P., N.M.J., T.M.S., and J.M.A. performed research; F.C.A.C., R.J.W. and R.L.K wrote the manuscript.

NOTES

The authors declare no competing financial interests.

ACKNOWLEDGMENT

The authors gratefully acknowledge support from the NSF (DMR-1410678 to R.J.W), and the National Institutes of Health (1R01-GM111932 to R.L.K.) Program and infrastructure support was from the National Institutes of Health National Center for Research Resources to the City College of New York (5G12-MD007603-30). R.L.K. is a member of the New York Structural Biology Center (NYSBC). NMR data collected at NYSBC was made possible by a grant from NYSTAR and ORIP/NIH facility improvement grant CO6RR015495. J.M.P. was the recipient of a fellowship award from the U.S. Department of Education Graduate Assistance in Areas of National Need (GAANN) Program in Biochemistry, Biophysics, and Biodesign at The City College of New York (PA200A150068).

ABBREVIATIONS

CEST, chemical exchange information transfer; IDP, intrinsically disordered protein; NMR, nuclear magnetic resonance; NOE, nuclear Overhauser effect; PFG, pulsed field gradient; MAS, magic angle spinning; SDM, spectral density mapping

REFERENCES

1. Cocciolone, A. J., J. Z. Hawes, M. C. Staiculescu, E. O. Johnson, M. Murshed, and J. E. Wagenseil. 2018. Elastin, arterial mechanics, and cardiovascular disease. Am J Physiol-Heart C 315:H189-H205.
2. Vrhovski, B., and A. S. Weiss. 1998. Biochemistry of tropoelastin. Eur. J. Biochem. 258:1-18.
3. Parker, K. H. 2009. A brief history of arterial wave mechanics. Med. Biol. Eng. Comput. 47:111-118.
4. Wagenseil, J. E., and R. P. Mecham. 2012. Elastin in Large Artery Stiffness and Hypertension. Journal of Cardiovascular Translational Research 5:264-273.
5. He, D., M. Chung, E. Chan, T. Alleyne, K. C. H. Ha, M. Miao, R. J. Stahl, F. W. Keeley, and J. Parkinson. 2007. Comparative genomics of elastin: Sequence analysis of a highly repetitive protein. Matrix Biol. 26:524-540.
6. Greenland, K. N., M. F. C. A. Carvajal, J. M. Preston, S. Ekblad, W. L. Dean, J. Y. Chiang, R. L. Koder, and R. J. Wittebort. 2018. Order, Disorder, and Temperature-Driven Compaction in a Designed Elastin Protein. Journal of Physical Chemistry B 122:2725-2736.
7. Tamburro, A. M., A. Pepe, and B. Bochicchio. 2006. Localizing alpha-helices in human tropoelastin: Assembly of the elastin "puzzle". Biochemistry 45:9518-9530.
8. Urry, D. W., T. Hugel, M. Seitz, H. E. Gaub, L. Sheiba, J. Dea, J. Xu, and T. Parker. 2002. Elastin: a representative ideal protein elastomer. Philosophical Transactions of the Royal Society of London Series B-Biological Sciences 357:169-184.
9. Pometun, M. S., E. Y. Chekmenev, and R. J. Wittebort. 2004. Quantitative observation of backbone disorder in native elastin. J. Biol. Chem. 279:7982-7987.
10. Hoeve, C. A. J., and P. J. Flory. 1974. ELASTIC PROPERTIES OF ELASTIN. Biopolymers 13:677-686.
11. Weis-Fogh, T. A., S. O. . 1970. New Molecular Model for the Long-range Elasticity of Elastin. Nature 227:4.
12. Gosline, J. M. 1978. HYDROPHOBIC INTERACTION AND A MODEL FOR ELASTICITY OF ELASTIN. Biopolymers 17:677-695.
13. Salvi, N., A. Abyzov, and M. Blackledge. 2019. Solvent-dependent segmental dynamics in intrinsically disordered proteins. Science Advances 5.

14. Gill, M. L., R. A. Byrd, and A. G. Palmer. 2016. Dynamics of GCN4 facilitate DNA interaction: a model-free analysis of an intrinsically disordered region. Phys. Chem. Chem. Phys. 18:5839-5849.
15. Khan, S. N., C. Charlier, R. Augustyniak, N. Salvi, V. Dejean, G. Bodenhausen, O. Lequin, P. Pelupessy, and F. Ferrage. 2015. Distribution of Pico- and Nanosecond Motions in Disordered Proteins from Nuclear Spin Relaxation. Biophys J 109:988-999.
16. Cavanagh, J., W. J. Fairbrother, A. G. Palmer, III, N. J. Skelton, J. Cavanagh, W. J. Fairbrother, A. G. Palmer, III, and N. J. Skelton. 1996. Experimental aspects of NMR spectroscopy.
17. Kay, L. E., D. A. Torchia, and A. Bax. 1989. Backbone Dynamics of Proteins as Studied by N-15 Inverse Detected Heteronuclear Nmr-Spectroscopy - Application to Staphylococcal Nuclease. Biochemistry 28:8972-8979.
18. Lipari, G., and A. Szabo. 1982. MODEL-FREE APPROACH TO THE INTERPRETATION OF NUCLEAR MAGNETIC-RESONANCE RELAXATION IN MACROMOLECULES .2. ANALYSIS OF EXPERIMENTAL RESULTS. Journal of the American Chemical Society 104:4559-4570.
19. Lipari, G., and A. Szabo. 1982. MODEL-FREE APPROACH TO THE INTERPRETATION OF NUCLEAR MAGNETIC-RESONANCE RELAXATION IN MACROMOLECULES .1. THEORY AND RANGE OF VALIDITY. Journal of the American Chemical Society 104:4546-4559.
20. Kaderavek, P., V. Zapletal, A. Rabatinova, L. Krasny, V. Sklenar, and L. Zidek. 2014. Spectral density mapping protocols for analysis of molecular motions in disordered proteins. Journal of Biomolecular Nmr 58:193-207.
21. Farrow, N. A., O. W. Zhang, A. Szabo, D. A. Torchia, and L. E. Kay. 1995. SPECTRAL DENSITY-FUNCTION MAPPING USING N-15 RELAXATION DATA EXCLUSIVELY. Journal of Biomolecular Nmr 6:153-162.
22. Wittebort, R. J., and A. Szabo. 1978. THEORY OF NMR RELAXATION IN MACROMOLECULES - RESTRICTED DIFFUSION AND JUMP MODELS FOR MULTIPLE INTERNAL ROTATIONS IN AMINO-ACID SIDE-CHAINS. Journal of Chemical Physics 69:1722-1736.
23. King, R., and O. Jardetzky. 1978. GENERAL FORMALISM FOR ANALYSIS OF NMR RELAXATION MEASUREMENTS ON SYSTEMS WITH MULTIPLE DEGREES OF FREEDOM. Chemical Physics Letters 55:15-18.
24. Khan, S. N., C. Charlier, R. Augustyniak, N. Salvi, V. Dejean, G. Bodenhausen, O. Lequin, P. Pelupessy, and F. Ferrage. 2015. Distribution of Pico- and Nanosecond Motions in Disordered Proteins from Nuclear Spin Relaxation. Biophysical Journal 109:988-999.
25. Smith, A. A., M. Ernst, B. H. Meier, and F. Ferrage. 2019. Reducing bias in the analysis of solution-state NMR data with dynamics detectors. Journal of Chemical Physics 151.
26. Lipari, G., A. Szabo, and R. M. Levy. 1982. PROTEIN DYNAMICS AND NMR RELAXATION - COMPARISON OF SIMULATIONS WITH EXPERIMENT. Nature 300:197-198.
27. Clore, G. M., A. Szabo, A. Bax, L. E. Kay, P. C. Driscoll, and A. M. Gronenborn. 1990. DEVIATIONS FROM THE SIMPLE 2-PARAMETER MODEL-FREE APPROACH TO THE INTERPRETATION OF N-15 NUCLEAR MAGNETIC-RELAXATION OF PROTEINS. Journal of the American Chemical Society 112:4989-4991.

28. Yao, S., J. J. Babon, and R. S. Norton. 2008. Protein effective rotational correlation times from translational self-diffusion coefficients measured by PFG-NMR. Biophysical Chemistry 136:145-151.
29. Marsh, J. A., and J. D. Forman-Kay. 2010. Sequence Determinants of Compaction in Intrinsically Disordered Proteins. Biophys. J. 98:2383-2390.
30. Martin, E. W., A. S. Holehouse, C. R. Grace, A. Hughes, R. V. Pappu, and T. Mittag. 2016. Sequence Determinants of the Conformational Properties of an Intrinsically Disordered Protein Prior to and upon Multisite Phosphorylation. Journal of the American Chemical Society 138:15323-15335.
31. Sterckx, Y. G. J., A. N. Volkov, W. F. Vranken, J. Kragelj, M. R. Jensen, L. Buts, A. Garcia-Pino, T. Jove, L. Van Melderen, M. Blackledge, N. A. J. van Nuland, and R. Loris. 2014. Small-Angle X-Ray Scattering- and Nuclear Magnetic Resonance-Derived Conformational Ensemble of the Highly Flexible Antitoxin PaaA2. Structure 22:854-865.
32. Kim, S., K.-P. Wu, and J. Baum. 2013. Fast hydrogen exchange affects N-15 relaxation measurements in intrinsically disordered proteins. Journal of Biomolecular Nmr 55:249-256.
33. Hwang, T. L., P. C. M. van Zijl, and S. Mori. 1998. Accurate quantitation of water-amide proton exchange rates using the Phase-Modulated CLEAN chemical EXchange (CLEANEX-PM) approach with a Fast-HSQC (FHSQC) detection scheme. J. Biomol. NMR 11:221-226.
34. Nguyen, D., L. Mayne, M. C. Phillips, and S. W. Englander. 2018. Reference Parameters for Protein Hydrogen Exchange Rates. Journal of the American Society for Mass Spectrometry 29:1936-1939.
35. Bai, Y. W., J. S. Milne, L. Mayne, and S. W. Englander. 1993. PRIMARY STRUCTURE EFFECTS ON PEPTIDE GROUP HYDROGEN-EXCHANGE. Proteins-Structure Function and Genetics 17:75-86.
36. Mori, S., P. C. M. vanZijl, and D. Shortle. 1997. Measurement of water-amide proton exchange rates in the denatured state of staphylococcal nuclease by a magnetization transfer technique. Proteins-Structure Function and Bioinformatics 28:325-332.
37. Greenland, K. N., M. F. Charmagne, A. Caryajal, J. M. Preston, S. Ekblad, W. L. Dean, J. Y. Chiang, R. L. Koder, and R. J. Wittebort. 2018. Order, Disorder, and Temperature-Driven Compaction in a Designed Elastin Protein. J. Phys. Chem. B 122:2725-2736.
38. Raju, K., and R. A. Anwar. 1987. PRIMARY STRUCTURES OF BOVINE ELASTIN-A, ELASTIN-B AND ELASTIN-C DEDUCED FROM THE SEQUENCES OF CDNA CLONES. Federation Proceedings 46:1989-1989.
39. Kjaergaard, M., and F. M. Poulsen. 2011. Sequence correction of random coil chemical shifts: correlation between neighbor correction factors and changes in the Ramachandran distribution. Journal of Biomolecular Nmr 50:157-165.
40. Grasberger, B. L., A. M. Gronenborn, and G. M. Clore. 1993. Analysis of the Backbone Dynamics of Interleukin-8 by N-15 Relaxation Measurements. J Mol Biol 230:364-372.
41. Abyzov, A., N. Salvi, R. Schneider, D. Maurin, R. W. H. Ruigrok, M. R. Jensen, and M. Blackledge. 2016. Identification of Dynamic Modes in an Intrinsically Disordered Protein Using Temperature-Dependent NMR Relaxation. Journal of the American Chemical Society 138:6240-6251.

42. Weiss, M. A., T. Ellenberger, C. R. Wobbe, J. P. Lee, S. C. Harrison, and K. Struhl. 1990. FOLDING TRANSITION IN THE DNA-BINDING DOMAIN OF GCN4 ON SPECIFIC BINDING TO DNA. Nature 347:575-578.
43. Cook, E. C., D. Sahu, M. Bastidas, and S. A. Showalter. 2019. Solution Ensemble of the C-Terminal Domain from the Transcription Factor Pdx1 Resembles an Excluded Volume Polymer. Journal of Physical Chemistry B 123:106-116.
44. Reichheld, S. E., L. D. Muiznieks, R. Lu, S. Sharpe, and F. W. Keeley. 2019. Sequence variants of human tropoelastin affecting assembly, structural characteristics and functional properties of polymeric elastin in health and disease. Matrix biology : journal of the International Society for Matrix Biology 84:68-80.
45. Baldock, C., A. F. Oberhauser, L. A. Ma, D. Lammie, V. Siegler, S. M. Mithieux, Y. D. Tu, J. Y. H. Chow, F. Suleman, M. Malfois, S. Rogers, L. A. Guo, T. C. Irving, T. J. Wess, and A. S. Weiss. 2011. Shape of tropoelastin, the highly extensible protein that controls human tissue elasticity. Proceedings of the National Academy of Sciences of the United States of America 108:4322-4327.
46. Brownaugsburger, P., C. Tisdale, T. Broekelmann, C. Sloan, and R. P. Mecham. 1995. IDENTIFICATION OF AN ELASTIN CROSS-LINKING DOMAIN THAT JOINS 3 PEPTIDE CHAINS - POSSIBLE ROLE IN NUCLEATED ASSEMBLY. Journal of Biological Chemistry 270:17778-17783.
47. Schraeder, C. U., A. Heinz, P. Majovsky, B. K. Mayack, J. Brinckmann, W. Sippl, and C. E. H. Schmelzer. 2018. Elastin is heterogeneously cross-linked. Journal of Biological Chemistry 293:15107-15119.
48. Roche, J., Y. Shen, J. H. Lee, J. F. Ying, and A. Bax. 2016. Monomeric A beta(1-40) and A beta(1-42) Peptides in Solution Adopt Very Similar Ramachandran Map Distributions That Closely Resemble Random Coil. Biochemistry 55:762-775.
49. Colvin, M. T., R. Silvers, Q. Z. Ni, T. V. Can, I. Sergeyev, M. Rosay, K. J. Donovan, B. Michael, J. Wall, S. Linse, and R. G. Griffin. 2016. Atomic Resolution Structure of Monomorphic A beta(42) Amyloid Fibrils. Journal of the American Chemical Society 138:9663-9674.
50. Potapov, A., W.-M. Yau, R. Ghirlando, K. R. Thurber, and R. Tycko. 2015. Successive Stages of Amyloid-beta Self-Assembly Characterized by Solid-State Nuclear Magnetic Resonance with Dynamic Nuclear Polarization. Journal of the American Chemical Society 137:8294-8307.
51. Kozel, B. A., H. Wachi, E. C. Davis, and R. P. Mecham. 2003. Domains in tropoelastin that mediate elastin deposition in vitro and in vivo. Journal of Biological Chemistry 278:18491-18498.
52. Krivokhizhina, T. V., and R. J. Wittebort. 2014. 2Q NMR of (H2O)-H-2 ordering at solid interfaces. Journal of Magnetic Resonance 243:33-39.
53. Daamen, W. F., T. Hafmans, J. H. Veerkamp, and T. H. van Kuppevelt. 2005. Isolation of intact elastin fibers devoid of microfibrils. Tissue Engineering 11:1168-1176.
54. Vallurupalli, P., G. Bouvignies, and L. E. Kay. 2012. Studying "Invisible" Excited Protein States in Slow Exchange with a Major State Conformation. Journal of the American Chemical Society 134:8148-8161.
55. Guenneugues, M., P. Berthault, and H. Desvaux. 1999. A method for determining B-1 field inhomogeneity. Are the biases assumed in heteronuclear relaxation experiments usually underestimated? Journal of Magnetic Resonance 136:118-126.

56. Chakrabarti, K. S., D. Ban, S. Pratihar, J. G. Reddy, S. Becker, C. Griesinger, and D. Lee. 2016. High-power H-1 composite pulse decoupling provides artifact free exchange-mediated saturation transfer (EST) experiments. Journal of Magnetic Resonance 269:65-69.
57. Carneiro, M. G., J. G. Reddy, C. Griesinger, and D. Lee. 2015. Speeding-up exchange-mediated saturation transfer experiments by Fourier transform. Journal of Biomolecular Nmr 63:237-244.
58. Gu, Q., H. Zhu, J. Li, X. Li, J. Hao, G. G. Wallace, and Q. Zhou. 2016. Three-dimensional bioprinting speeds up smart regenerative medicine. Natl Sci Rev 3:331-344.
59. Farrow, N. A., R. Muhandiram, A. U. Singer, S. M. Pascal, C. M. Kay, G. Gish, S. E. Shoelson, T. Pawson, J. D. Forman-Kay, and L. E. Kay. 1994. Backbone dynamics of a free and phosphopeptide-complexed Src homology 2 domain studied by 15N NMR relaxation. Biochemistry 33:5984-6003.
60. Ochsenbein, F., R. Guerois, J. M. Neumann, A. Sanson, E. Guittet, and C. van Heijenoort. 2001. N-15 NMR relaxation as a probe for helical intrinsic propensity: The case of the unfolded D2 domain of annexin I. J Biomol NMR 19:3-18.
61. Zhang, Q. W., H. M. Zhang, K. V. Lakshmi, D. K. Lee, C. H. Bradley, and R. J. Wittebort. 1998. Double and triple resonance circuits for high-frequency probes. J Magn Reson 132:167-171.